Journal of Molecular Structure 1119 (2016) 286–295

Contents lists available at ScienceDirect

Journal of Molecular Structure

journal homepage: http://www.elsevier.com/locate/molstruc

Theoretical and experimental comparative study of a derivative from 2-pyridinecarboxaldehyde which exhibits configurational dynamics

Mónica A. Gordillo [a], Mónica Soto-Monsalve [b], Gustavo Gutiérrez [c], Richard F. D'vries [d], Manuel N. Chaur [a, *]

[a] *Departamento de Química, Universidad del Valle, 760032, Cali, Colombia*
[b] *Instituto de Química de São Carlos, Universidade de São Paulo, 13566-590, São Carlos, Brazil*
[c] *Departamento de Ciencias Farmacéuticas, Universidad Icesi, Cali, Colombia*
[d] *Instituto de Física de São Carlos, Universidade de São Paulo, 13566-590, São Carlos, Brazil*

ARTICLE INFO

Article history:
Received 5 December 2015
Received in revised form
17 April 2016
Accepted 18 April 2016
Available online 21 April 2016

Keywords:
Acylhydrazone
Photoisomerization
NMR
DFT
HF
X-ray crystal diffraction

ABSTRACT

The (E)-4-nitro-N′-(pyridine-2-ylmethylene)benzohydrazide, a derivative from 2-pyridinecarboxaldehyde, displays E/Z isomerization induced by ultraviolet radiation in which the process of photoisomerization was evidenced and followed by 1D ^{1}H NMR. The structure of the compound was determined by FT-IR and NMR techniques and confirmed by single-crystal X-ray diffraction. The results in terms of bond angle and length, chemical shift (^{13}C and ^{1}H) and vibrational frequencies obtained experimentally were compared to computed values at two levels of theory (Restricted Hartree–Fock and Density Functional Theory) using different basis set. The understanding of spectroscopy and dynamic properties of these type of compounds is of importance in view of their potential use in molecular machines and electronic devices.

1. Introduction

Acyl-hydrazones exhibit a large number of applications, among them, we can highlight the information storage. This functional group presents a weak double bond that is able to allow constitutional changes, through substituents interchange [1] establishing itself as a long term information storage strategy. Furthermore, acyl-hydrazones presents dynamical responses to diverse types of stimulus, both chemical (pH and conformational changes induced by metallic ions) and physical (pressure, heat and radiation) [2–5].

From a wide variety of possible stimuli, probably the most feasible is the luminous radiation (especially in UV spectral region) since the energy investment is lower compared to heat or pressure application and it has a higher practical applicability, interruption of stimulus once the system has reached the expected response using changes in the pH solution or the addition of metallic ions, is one of them and systems showing this on/off behavior are commonly known as molecular switches. Herein we present the synthesis, photochemistry and spectroscopy comparison to theoretical calculations of an acyl-hydrazone derivative from 2-pyridinecarboxaldehyde capable of responding to UV radiation through a process of reversible E/Z photoisomerization where the product is stabilized by an intramolecular hydrogen bond.

2. Experimental and computational methods

The starting materials were purchased from Sigma–Aldrich and Alfa Aesar, they were used without any further purification. ^{1}H and ^{13}C NMR spectra were taken in a 400 MHz Bruker Ultra Shield spectrometer and the FT-IR spectra were recorded on a Shimadzu FTIR-8400 instrument.

2.1. Synthesis A-1

An equivalent of 2-pyridinecarboxaldehyde was added to an ethanol solution (7 mL) of 4-nitrobenzohydrazide (1eq) and a trace amount of glacial acetic acid. This mixture was heated under reflux for 3 h, the appearance of precipitate was observed after the first 10 min of reaction. The white solid was filtered and recrystallized

---

* Corresponding author.
E-mail address: manuel.chaur@correounivalle.edu.co (M.N. Chaur).

http://dx.doi.org/10.1016/j.molstruc.2016.04.055

from ethanol (96% yield). M. p.: 227–228 °C. FT-IR (ν/cm-1): 3221 (N–H), 1659 (C=O), 1595(C=N). ^{1}H NMR (400 MHz, DMSO-d_6), δ/ppm: 12.31 (s, 1 H), 8.64 (d, J = 4.29 Hz, 1 H), 8.49 (s, 1 H), 8.39 (d, J = 8.59 Hz, 2 H), 8.17 (d, J = 8.59 Hz, 2 H), 8.01 (d, J = 7.80 Hz, 1 H) 7.94–7.87 (m, 1 H) 7.47–7.42 (m, 1 H). ^{13}C NMR (100.60 MHz, DMSO-d_6), δ/ppm: 161.76, 152.96, 149.59, 149.38, 149.12, 138.80, 136.95, 129.26, 124.65, 123.69, 120.08. Elemental analysis calculated. (%) for $C_{13}H_{10}N_4O_3$: C, 57.78; H, 3.73; N, 20.73; found: C, 57.86; H, 3.72; N, 20.62.

2.2. Photoisomerization of (E)-4-nitro-N'-(pyridine-2-ylmethylene) benzohydrazide

A solution of *A-1* (in DMSO-d_6), in a NMR Quartz tube was placed 20 cm from a mercury-vapor lamp and was irradiated. Spectra were taken every 10 min starting from zero up to 90 min.

2.3. Crystallography

Single crystal X-Ray diffraction data were collected at Bruker

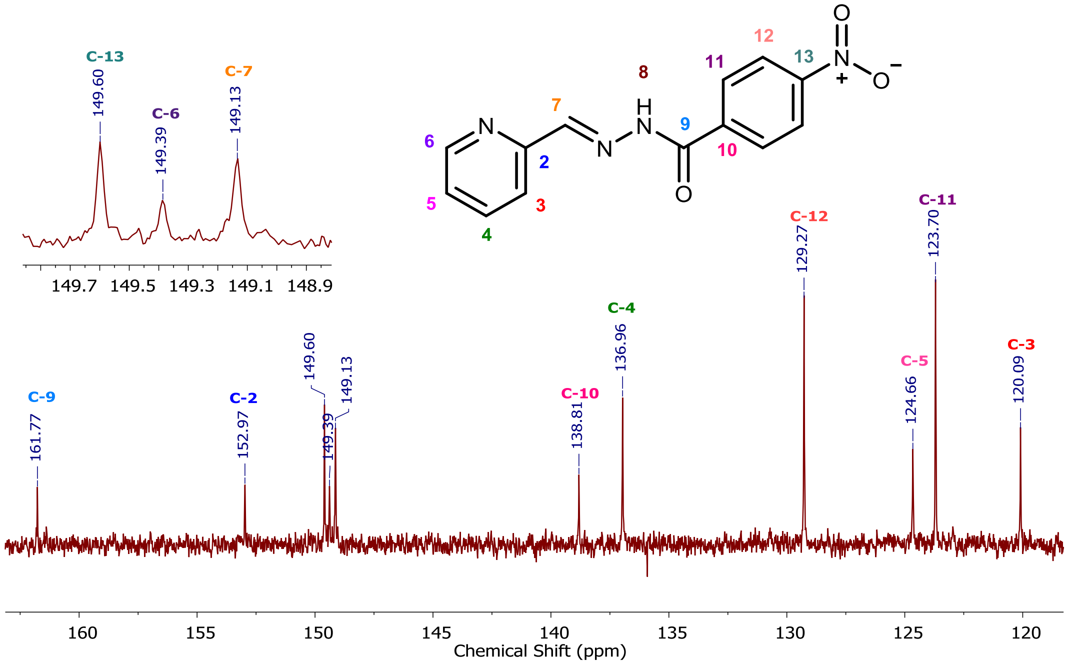

Fig. 1. ^{13}C NMR signals assignments of *A-1*.

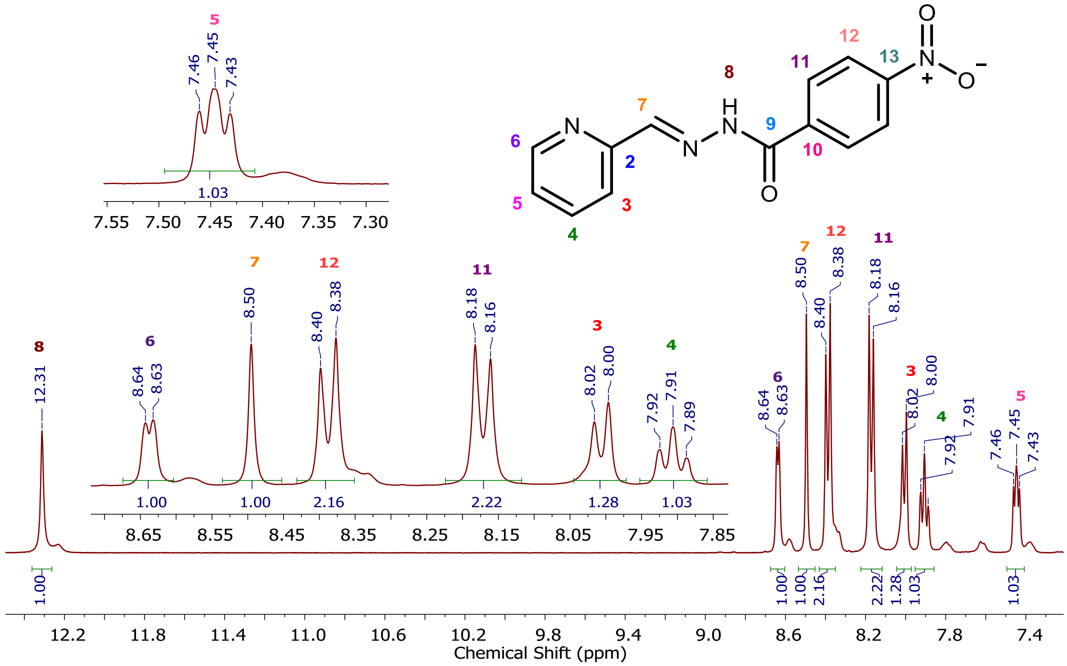

Fig. 2. ^{1}H NMR signals assignments of *A-1*.

APEX-II CCD diffractometer with MoKα radiation (λ = 0.71073 Å) monochromated by graphite at 298 K. Data integration, cell and cell parameters determination was carried out using Bruker SAINT [6]. The structure was solved using the software SHELXS-2013, and then refined using SHELXL-2013, included in WinGX [7] and Olex2-1.2 [8]. CCDC 1424366 contains the supplementary crystallographic data for this paper.

2.4. Computational details

The theoretical studies were performed employing GaussView 5.0 [9] as graphic interface and Gaussian 09 [10] for computing. Determination of minimum energy geometry at ground state was carried out at two levels of theory: Density Functional Theory (RB3LYP method) and Restricted Hatree—Fock testing accuracy of three basis set: 6-31G+, 6-311G+ and 6-311G (d, p). Cartesian coordinates for optimized structures are provided in supplementary materials (see Tables S1–S12). As expected, the best theoretical—experimental correlation was achieved with the DFT: B3LYP method [11], for this reason DFT: B3LYP/6-311G (d, p) is used henceforth for frequency calculations where the absence of imaginary frequencies confirmed that the minimum energy structure was achieved [12]. NMR ^{13}C and ^{1}H chemical shift using TMS DFT: B3LYP/6-311G+ (d, p) internal Gaussian's 09 reference, additionally, DFT results was contrasted with RHF/6-311G (d, p) calculations. All chemical shifts were calculated using gauge-including atomic orbitals (GIAO) method without any solvent or solvation effect considerations.

3. Results and discussion

3.1. Nuclear magnetic resonance studies and computational chemical shifts calculations

Firstly, the molecular structure determination was carried out by NMR (^{1}H and ^{13}C), the assignments presented in Figs. 1 and 2 are supported both by literature information about typical chemical shift as well as experiments of homo and heteronuclear correlation NMR spectroscopy (COSY, HMBC and HSQC). Theoretical chemical shift for ^{13}C and ^{1}H was performed at two theory levels (DFT: B3LYP and RHF) using 6-311G (d, p) basis set with internal Gaussian's reference TMS DFT: B3LYP/6-311G+ (d, p) using gauge-including atomic orbitals (GIAO) method.

^{13}C NMR chemical shifts show an acceptable correlation with experimental data (see Table 1). DFT: B3LYP/6-311G (d, p) computed values show a clear tendency to overestimate, where biggest discrepancy comes from signal C-11: experimental spectrum presents two equivalent carbons (strong signal at 123.70 ppm) while theoretical spectrum shows two different signals (126.92 ppm and 135.85 ppm, 2.95 and 9.82% error, respectively). On the other hand, RHF/6-311G (d, p) computed values are totally underestimated and show significantly lower accuracy.

The biggest difference between experimental and calculated data was presented in C-7 signal, 149.13 ppm experimental value respect to 129.67 ppm computed value (13.05 absolute percent error), even the second greatest deviation in C-5 signal is near to the biggest deviation in DFT: B3LYP/6-311G (d, p) calculations (experimental 124.66 ppm respect to 112.92 ppm computed value, 9.42 absolute percent error).

Table 1
NMR chemical shifts (^{13}C and ^{1}H): theoretical-experimental comparison.

^{13}C NMR chemical shifts		
Experimental (ppm)	DFT: B3LYP/6-311G (d, p)	RHF/6-311G (d, p)
149.39	155.43	149.08
124.66	126.00	112.92
136.96	138.90	131.93
120.09	128.28	113.02
152.97	157.34	144.52
149.13	143.39	129.67
161.77	161.17	149.31
138.81	144.61	134.38
123.70	135.85	123.80
129.27	128.14	119.27
149.60	155.67	138.87
129.27	126.92	117.80
Linear regression parameters		
Intercept	16.379	5.7139
Slope	0.9032	0.8978
R^2	0.8764	0.8527
^{1}H-NMR chemical shifts		
Experimental (ppm)	DFT: B3LYP/6-311G (d, p)	RHF/6-311G (d, p)
8.64	9.00	8.58
7.45	7.09	6.80
7.91	7.66	7.53
8.01	7.12	6.70
8.50	7.70	7.14
12.31	8.20	6.64
8.17	8.36	8.07
8.39	8.46	8.40
8.17	7.52	7.23
8.39	8.37	8.31
Linear regression parameters[a]		
Intercept	5.4683	5.9871
Slope	1.6481	1.6816
R^2	0.7377	0.6814

[a] Regression data set excluding signals 8 and 9.

Table 2
Crystal data and structure refinement parameters.

Identification code	*A-1*
Empirical formula	$C_{13}H_{12}N_4O_4$
Formula weight	288.27
Temperature/K	296 (2)
Crystal system	Triclinic
Space group	P−1
a/Å	7.3756 (3)
b/Å	13.1398 (5)
c/Å	14.7835 (6)
α/°	109.128 (2)
β/°	90.531 (2)
γ/°	101.107 (2)
Volume/Å^3	1324.21 (9)
Z	4
ρ_{calc} mg/mm3	1.446
m/mm^{-1}	0.110
F (000)	600
Crystal size/mm^3	0.242 × 0.175 × 0.112
2θ range for data collection	1.462–26.494°.
Index ranges	$-9 \le h \le 9$, $-16 \le k \le 16$, $-17 \le l \le 18$
Reflections collected	16449
Independent reflections	5290 [R (int) = 0.0195]
Data/restraints/parameters	5290/0/403
Goodness-of-fit on F^2	1.024
Final R indices [I > 2sigma(I)]	R1 = 0.0465, wR2 = 0.1191
R indices (all data)	R1 = 0.0724, wR2 = 0.1377
Largest diff. Peak/hole/e Å^{-3}	0.213/−0.204 e Å^{-3}

Furthermore, prediction capacity of these theory level and basis set combination for ^{1}H NMR chemical shifts was unacceptable. The main source of error is signal **8** (see Fig. 2), N—H proton appears at 12.31 ppm in experimental ^{1}H NMR spectrum but at 8.20 ppm (DFT: B3LYP/6-311G (d, p), 33.41% error) and 6.64 ppm (RHF/6-311G (d, p), 46.06% error) in computed spectra. This sharp discrepancy may not be entirely related to the accuracy of the computational method used, since the variability of this particular signal in ^{1}H

NMR experiments is remarkable, in fact, it is highly dependent on the solvent in which the spectrum was taken [13], similarly H–C═N proton (signal 7 in Fig. 2 and 8.50 ppm) shows significant deviation at both levels of theory: 7.70 ppm (DFT: B3LYP/6-311G (d, p), 9.42% error) and 7.14 ppm (RHF/6-311G (d, p), 16.00% error) explained by a high electronic environment dependence since this signal can appear from ~ 6–9.50 ppm [14]. Finally, another important source of error, as well as in computed ^{13}C NMR chemical shifts, was the presence of separate signals for equivalent protons in the theoretical spectrum: signal 11, a doublet at 8.16–8.18 ppm appears in theoretical spectra like two signals at 8.36 ppm and 7.52 ppm, 2.33 and 7.96% error, respectively for DFT: B3LYP/6-311G (d, p) calculations and 8.07 ppm and 7.23 ppm, 1.22 and 11.51% error for RHF/6-311G (d, p).

3.2. *Crystallographic study and optimized structure*

Non-hydrogen atoms of the molecules were clearly resolved, and the full-matrix least-squares refinements of these atoms with anisotropic thermal parameters were carried out. All hydrogen atoms were stereochemically positioned and refined with the riding model [15]. Hydrogen atoms bonded to N and O atoms were localized in the density map. ORTEP diagram was prepared with ORTEP-3 [16]. Mercury [17] software was used to prepare the artwork. Crystal data, data collection and structure refinement details are summarized in Table 2.

Compound *A-1* crystalized in the triclinic space group P-1. There are two molecules of *A-1* per asymmetric unit, where the pyridinic ring has rotated over the C_{14}–C_{19} or C_5–C_6 bond generating two different conformers. This behavior generates a pseudo-translational symmetry element in (0.027, 0.508 and 0.012). When both conformers are refined in the same configuration, R_1 and WR2 values are 0.0915 and 0.2166 respectively, compared with the values (0.0465 and 0.1191) obtained when the structure was refined as different conformers. It means that the model of two different conformers is closer to the experimental data.

Nitro and amide groups for the conformer 2 present torsion angles of 1.28 (1)° and 158.18 (1)° for C_{12}–C_{11}–N_4–O_2 and O_1–C_7–C_8–C_9 bonds, respectively; in conformer 1, the same torsion angles are −14.65 (1)° and −172.94 (1)° for C_{25}–C_{24}–N_8–O_5 and O_4–C_{20}–C_{21}–C_{26} bonds respectively (see Fig. 3).

The structure exhibits strong hydrogen bonds between *A-1* and water molecules. These interactions enable to join the conformers, in an alternating way, giving rise to infinite chains along [010]. Hydrogen bonds parameters are listed in Table 3. O2w − H4w ··· N5, O2w − H3w ··· O4 with a distance of 2.9848 (1) Å, 2.8289 (1) Å respectively, form a R^2_2 (10) motif. N3 − H3 ··· O2w, O1w − H1w ··· O1 and N7 − H7A ··· O1w form graph sets type D^2_2 (4) (see Fig. 4).

π–π stacking interactions between pyridinic and benzene rings are observed among molecules of the same conformer. The first conformer presents inter-centroid distances (cg1···cg2 and cg2···cg1) of 3.7562 (2) Å and 3.7405 (2) Å, while the second conformer presents distances (cg3···cg4 and cg4···cg3) of 3.6582 (1) Å and 3.7560 (2) Å, joining the chains along [100] direction (see Fig. 5).

Very weak C–H ··· O interactions between C2–H2 ··· O3 and C17 − H17 ··· O6 with a distance of 3.530 (1) Å and 3.492 (1) Å, respectively, give raise to infinite chains along the [111] direction to complete the 3D supramolecular crystal packing (see Fig. 6 and 7).

The Hirshfeld surface shows the susceptible areas to strong and

Table 3
Hydrogen bonds for *A-1*.

D − H ... A	d (D − H)	d (H ... A)	d (D ... A)	<(DHA)
O (1W)–H (1W) ... N (2)[a]	0.82 (3)	2.59 (3)	3.226 (2)	135 (3)
O (1W)–H (1W) ... O (1)[a]	0.82 (3)	2.08 (3)	2.842 (2)	155 (3)
O (1W)–H (2W) ... O (2W)[b]	0.79 (4)	2.41 (4)	3.170 (3)	161 (4)
N (3)-H (3A) ... O (2W)[c]	0.87 (2)	2.02 (2)	2.887 (3)	173 (2)
N (7)-H (7A) ... O (1W)[d]	0.87 (3)	2.02 (2)	2.860 (3)	164 (2)

[a] −x,−y,−z+1.
[b] −x+1,−y+1,−z+1.
[c] −x,−y+1,−z+1.
[d] 1−x,−y,1−z.

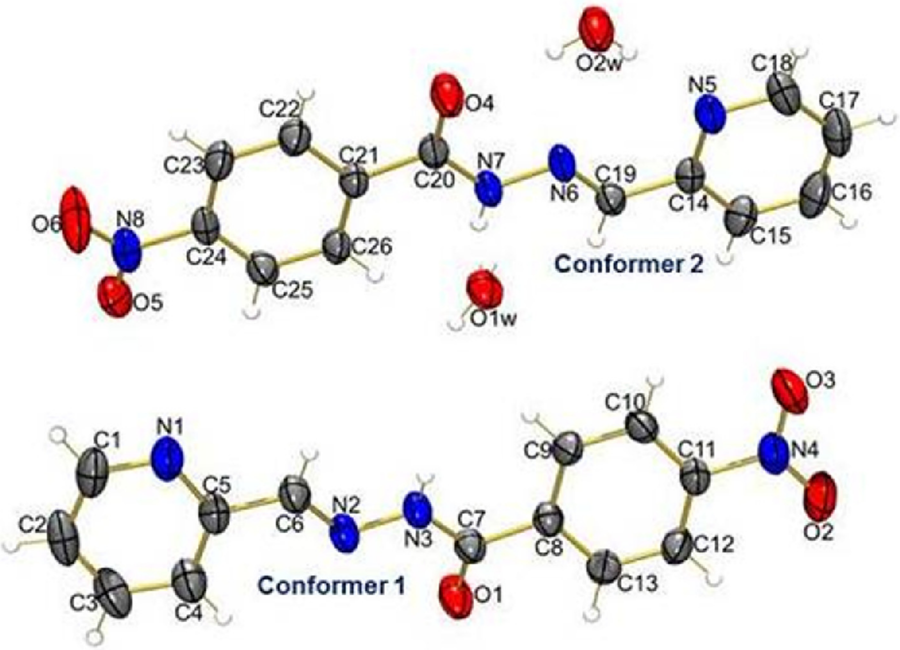

Fig. 3. ORTEP representation of asymmetric unit of *A-1*. Thermal ellipsoids are drawn at 50% probability level.

weak contacts (see Fig. 8). The map of shape index on the Hirshfeld surface can be used to find complementary regions (concave red curvature for H acceptor groups and convex blue curvature for H donor groups) where two molecular Hirshfeld surfaces touch each other [18,19]. In this case, concave red curvature is placed around N and O atoms with free electron pairs. The convex blue curvature was found mainly in N–H and C–H region. Over the aromatic rings are observed blue and red regions that evidence the π-π stacking.

The fingerprints graphic (see Fig. 9) presents a symmetric behavior where the two sharp peaks projecting downwards of the fingerprint are due to the strong O···H and N···H interactions [20]. The most important interaction can be evaluated by overlapping contributions from the hydrogen interactions which includes N···H, H···N, H···H, O···H and C···H. This analysis shows that the strong O···H interactions contribute the most to the Hirshfeld Surface with 33.1% followed by H···H with 29.7%. C···C that corresponds to π-π stacking contributes with 12.1%, while the strong N···H interactions contribute with 7.5% and C···H with 8.8%.

Optimization of molecular structure was performed at two levels of theory: Density Functional Theory (DFT) and Restricted Hartree–Fock (RHF), using different basis sets.

In concordance to experimental results, all computed structures show a essentially planar configuration in acyl-hydrazone bridge and pyridine ring while the nitro-benzene moiety shows a notable deviation respect to the observed planarity in molecular structure determined via single-crystal X-ray diffraction (see Fig. 10b). These deviations represent dihedral angles between acyl-hydrazone bridge and benzene ring (N_3–C_7–C_8–C_9) of 152.3° and (N_3–C_7–C_8–C_{13}) −30.4° (DFT B3LYP/6-311G) in contrast to experimental values −174.0° and 6.6°, respectively. Since this optimized geometry was calculated for an isolated molecule in gas phase, the conformational difference is explained by the absence of intermolecular interactions that modifies the orientation in solid state (see Fig. 10).

Another trend in computed optimized geometries is the presence of a possible resonant structure evidenced in dotted line over N_3–C_7 bond (see Fig. 10a) probably product of a keto-enol tautomerization process [21]. This explanation is supported in ^1H NMR subtle evidence, where small shoulders next to almost all signals, suggest the existence of the tautomer in mention (see Fig. 2).

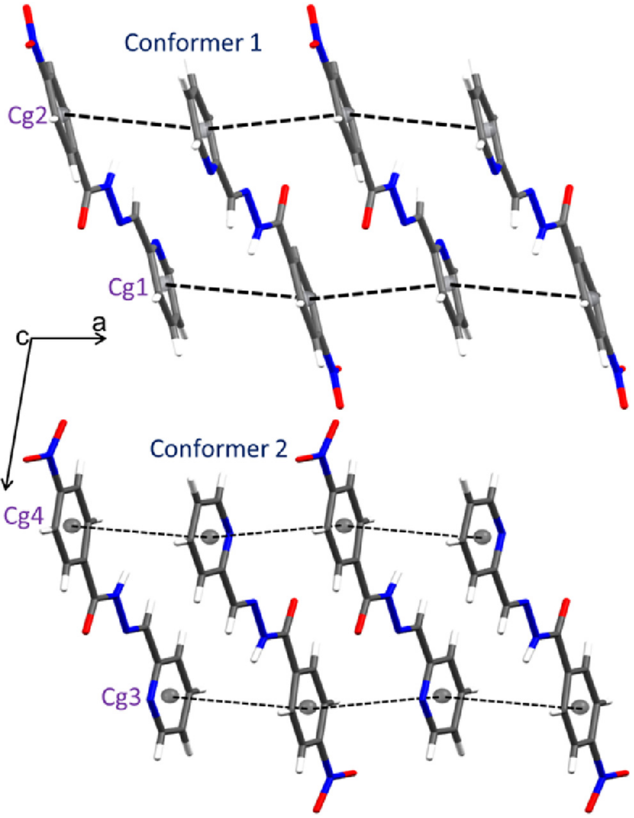

Fig. 5. π- π stacking between pyridinic and benzene rings and growth along [100] direction.

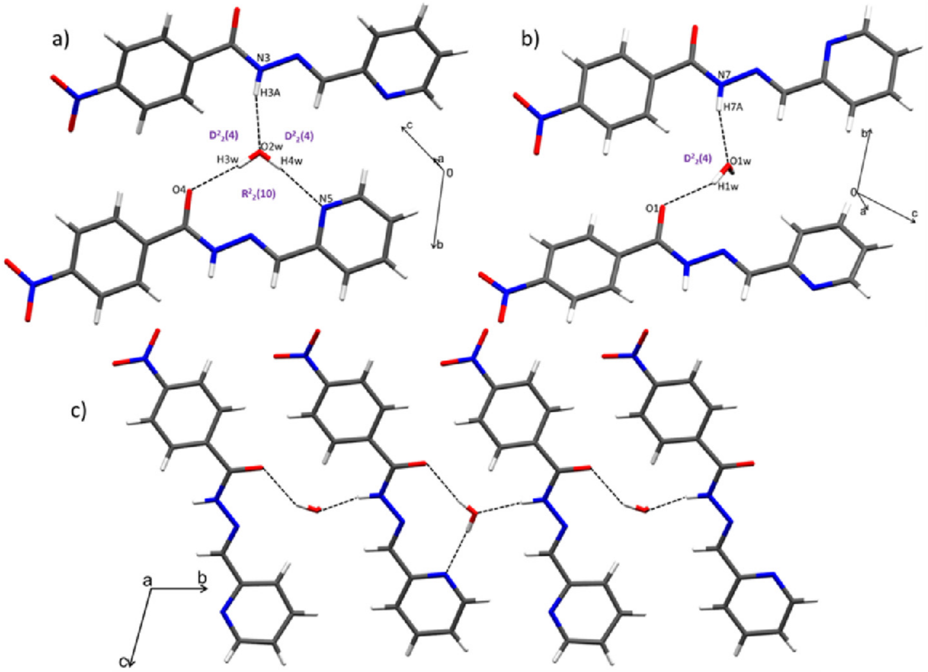

Fig. 4. a) Hydrogen bonds between *A-1* and water forming a R^2_2 (10) and two D^2_2 (4) graph sets, b) Hydrogen bonds between *A-1* and water forming a D^2_2 (4) graph set and c) Infinite chain along [010] direction.

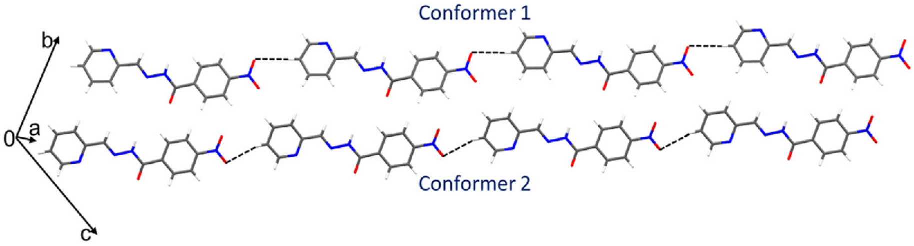

Fig. 6. Weak C − H … O interactions and growth along [111] direction.

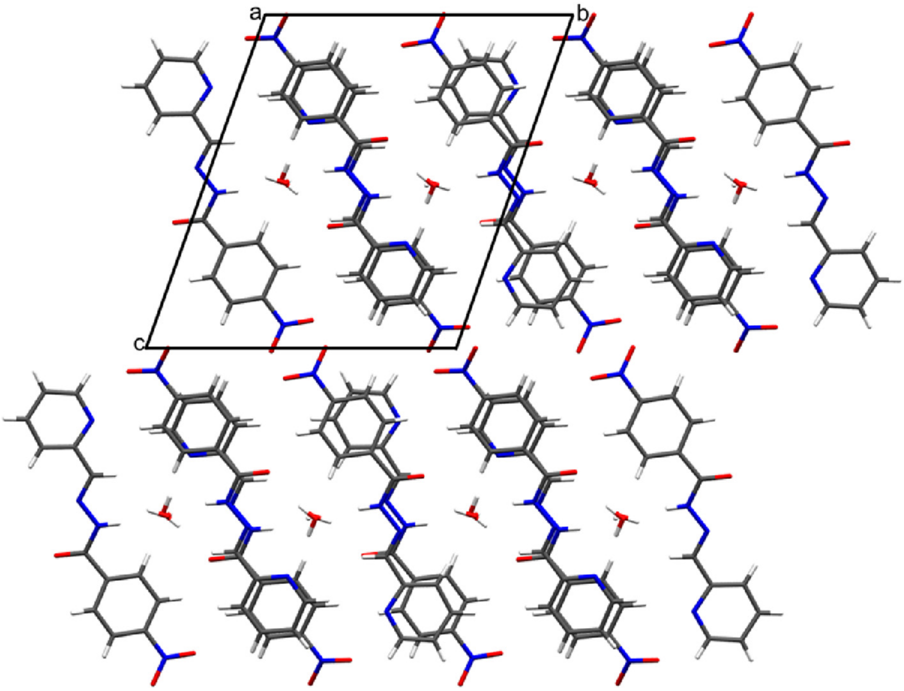

Fig. 7. Crystal packing representation of *A-1* view along [100] direction.

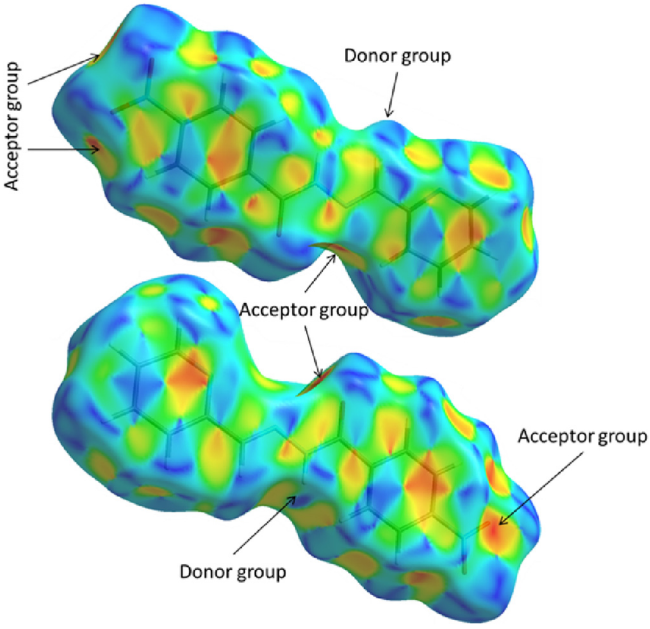

Fig. 8. Hirshfeld surface of *A-1* without water.

For the purpose of determining the suitability of the application of computational methods for predicting bond length and angle in this particular system, two levels of theory and different basis set were tested and compared with selected crystallographic data values via linear regression using experimental data as independent variable and computed values as response, which are shown below in Table 4. Selected geometrical parameters used in linear regressions analysis are detailed in the supplementary information (see Tables S13 and S14).

Linear regression provides important information for evaluation of the general accuracy of these calculations because the slope is a proportion between experimental and theoretical data variation [22], estimating in this way the difference between both data sets. A perfect experimental-computed data correlation represents a slope equal to one, values greater or less than one represent over- or underestimated response, respectively. On the other hand, the intercept value provides quantitative information about deviation because this parameter is defined as the value of the response when the input variable is zero. In the same vein, the intercept determines, in average, in what extent the answer is over or underestimated. Finally, R^2 value provides the percentage of response variability that is explained by the variation of the independent variable, an indirect measure of the reliability of the parameters: slope and intercept [23].

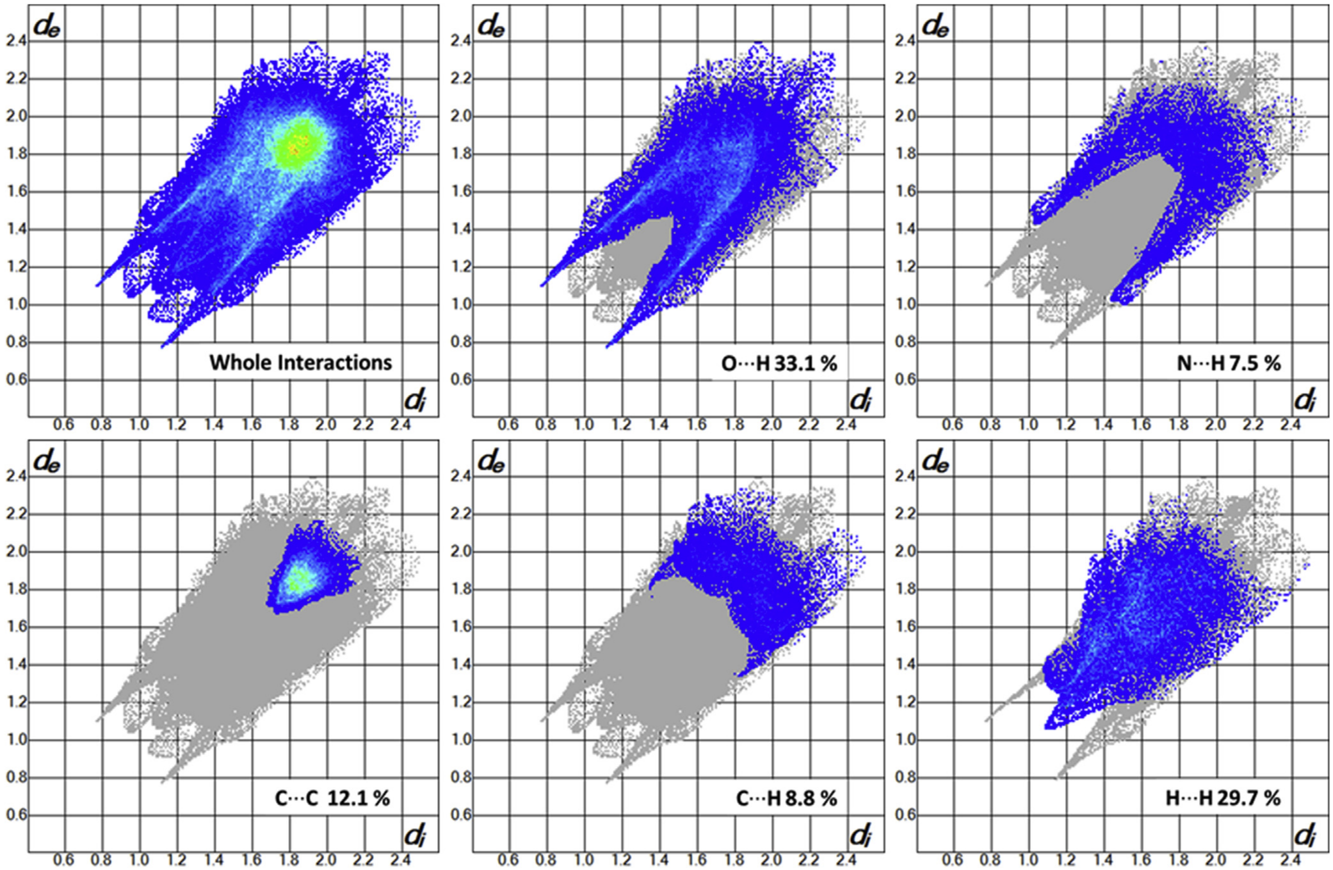

Fig. 9. Bidimensional fingerprint plot for whole molecule and O···H, N···H, N···H, C···C, C···H and H···H close contacts.

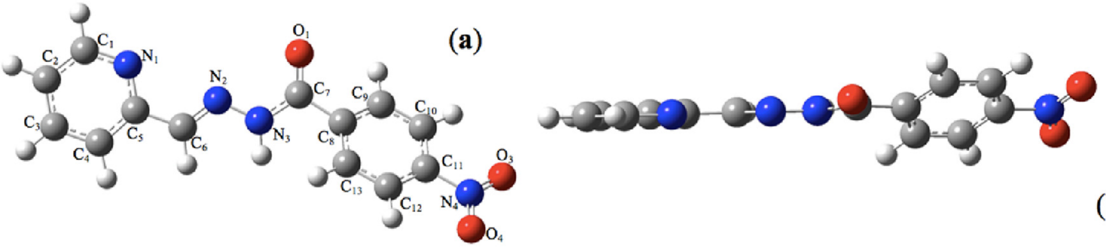

Fig. 10. Optimized geometry for conformer 2: DFT: B3LYP 6-311G (d, p). (**a**) Frontal view; (**b**) Side view.

For conformer 2, the Restricted Hartree–Fock approximation showed considerable accuracy using 6-311G (d, p) basis set for determining the bond length with a lower computational cost, while DFT showed a high accuracy in the determination of the bond angles, however, since both of the calculations cannot be carried out separately, the level of theory with the greatest correlation was DFT, thus, DFT: B3LYP/6-311G (d, p) is a suitable option for theoretical prediction of molecular structure: $R^2 = 0.99272$ and 0.97648 for bond angles and lengths, respectively. The biggest discrepancy at this level of theory and basis set was the $N_3{-}C_7$ bond length (calculated length = 0.040 Å longer than X-ray determinated length, 2.97% error) and $N_2{-}N_3{-}C_7$ bond angle (calculated angle is 3.1° higher than X-ray determinated angle, 2.63% error).

On the other hand, structure optimization for conformer 1 showed similar theoretical–experimental correlation trends regarding conformer 2 (see Table 4). Nevertheless, the correlation for bond angle calculations showed a notably minor quality fit at all basis set and levels of theory. These differences between one or other conformer using the same optimization routine are probably associated with intrinsic stability of each conformation, this affirmation is supported by a subtle minor energy for conformer 2 and one order of magnitude of difference between RMS gradients (see Table 5.) pointing out that the structure for this conformer is closer to an absolute optimization than conformer 1 and therefore has a greater stability.

3.3. FT-IR vibrational analysis

The Infrared spectrum was recorded on a Shimadzu FTIR 8400 spectrophotometer. The condensation reaction between 2-pyridinecarboxaldehyde and 4-nitrophenylhydrazine was evidenced by the disappearance of a 2823–2841 cm^{-1} band corresponding to aldehyde C–H stretching and occurrence of a weak signal at 3062 cm^{-1} corresponding to C–H stretching in the N=CH

Table 4
Linear regression fit parameters for bond angle and length data correlation.

Theory level/Basis set	Conformer 2			Conformer 1		
	Slope	Intercept	R^2	Slope	Intercept	R^2
Bond length linear regressions						
RHF/6-31G+	0.9258	0.0898	0.99878	0.9211	0.0981	0.99936
DFT: B3LYP/6-31G+	0.8699	0.1846	0.99065	0.8607	0.1992	0.99275
RHF/6-311G+	0.9301	0.0836	0.99804	0.9235	0.0934	0.99884
DFT: B3LYP/6-311G+	0.8910	0.1407	0.99870	0.8764	0.1770	0.99325
RHF/6-311G (d, p)	1.0846	−0.1339	0.99332	1.0829	0.1305	0.99462
DFT: B3LYP/6-311G (d, p)	1.0225	−0.0336	0.97648	1.0179	0.0261	0.97884
Bond angle linear regressions						
RHF/6-31G+	0.7665	28.247	0.90213	0.6880	37.637	0.75325
DFT: B3LPY/6-31G+	0.9189	9.8312	0.98534	0.8268	20.934	0.94956
RHF/6-311G+	0.8433	18.944	0.95548	0.6972	36.527	0.76970
DFT: B3LYP/6-311G+	1.0182	2.0043	0.99625	0.8190	21.885	0.94862
RHF/6-311G (d, p)	1.2378	28.218	0.97241	1.0681	7.7680	0.88256
DFT:B3LYP/6-311G (d, p)	1.2710	32.207	0.99272	1.1000	11.594	0.92603

Table 5
Energy and RMS gradient values for both conformers.

Level of theory/Basis set	Conformer 2		Conformer 1	
	Energy[a]	RMS gradient	Energy[a]	RMS gradient
RHF/6-311G (d, p)	−940.55564	0.00001685	−940.565634	0.00000861
DFT: B3LYP/6-311G (d, p)	−945.88865	0.00000062	−946.201184	0.00000851

[a] Energy values are provide in *Hartrees*.

moiety, finally the disappearance of H—N—H symmetrical stretch signal in 4-nitrophenylhydrazine IR spectra at 3322 cm^{-1} corresponding to hydrazine also notes that the expected reaction occurred.

Computed frequencies using DFT: B3LYP/6-311G (d, p) were scaled (scale factor = 0.9679) [24] and compared with experimental data below in Table 6.

Vibrational frequencies correlation between experimental and computed frequencies evaluated via linear regression. Experimental data showed good agreement ($R^2 = 0.99259$), with a slight tendency to underestimate (slope = 0.9812 and intercept = 43.86). Largest deviation found comparing the two sets of data occurs in the bond stretching frequency N—N (5.98% error).

Table 6
Selected signals in experimental IR and correlation with computed frequencies.

Assignments	Experimental/cm^{-1}	DFT: B3LYP/6-311G (d, p)
O=N=O *Asym. Strech*	1543.05	1598.19
O=N=O *Sym. Strech*	1344.38	1380.20
N—H *Strech*	3221.12	3372.56
C—H stretch (N=CH)	3062.96	2909.69
C=O *Strech*	1658.78	1726.99
C=N *Strech*	1595.13	1623.50
C—H stretch (Ar—H)	3221.12	3123.25
N—H Rock	1514.12	1506.26
N—N Strech	1056.99	1120.17
Py skeletal vibration	601.79	614.79
Benzene skeletal vibration	661.58	621.97

3.4. *Photoisomerization*

A solution of *A-1* in DMSO-d_6 was irradiated by a mercury vapor lamp and several spectra were taken trough time (see Fig. 11).

From the figure above we can observe the apparition of new signals after 5 min of UV light irradiation, which is an indicative of *Z* isomer formation. The percentages were calculated using proton **8** (—NH—) as a reference due to the appearance of a new – isolated and easy to integrate-signal at 15.84 ppm corresponding to the —NH— proton, which is part of an hydrogen bond in the metastable *Z* isomer. From this data and the rate law expression $rate = k[E_{isomer}]^2$, we found that the conversion from *E* to *Z* isomer follows a second order kinetics, having a rate constant of $k = 0.147\ M^{-1}\ min^{-1}$.

Here we cannot say if the photoisomerization proceed via the rotation or inversion mechanism since it was not performed in a wide variety of solvents. However, this mechanism has been extensively studied for imines and hydrazones (lesser extent), having different results, some suggest that inversion is the mechanistic pathway followed for this kind of compounds, others supported in theoretical calculations have found that photoisomerization may occur by out-of-plane rotation. Therefore, more experimentation is needed in order to completely understand

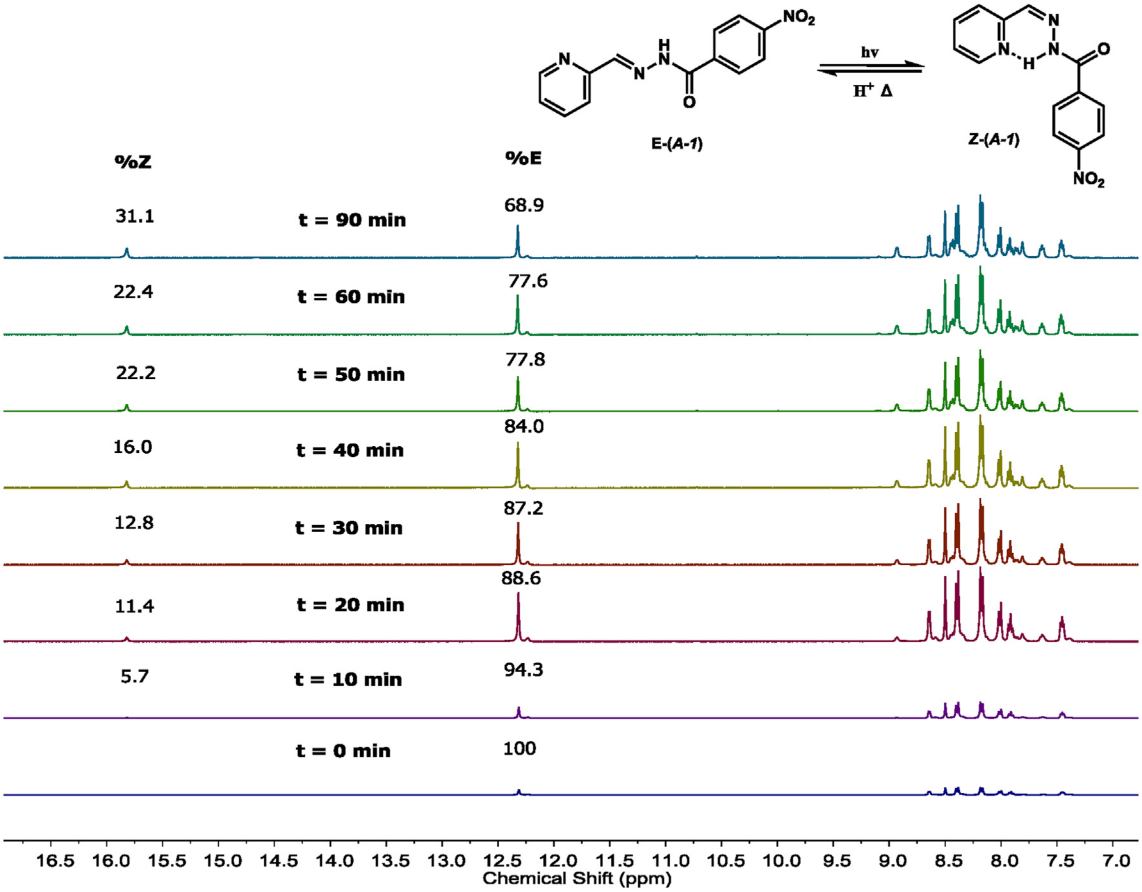

Fig. 11. 1D ^{1}H NMR results of photoisomerization assay in DMSO-d_6.

the *E* to *Z* isomerization mechanism in hydrazones [25,26] For acylhydrazones, nevertheless, it is known that photoisomerization proceeds through the weakening of the C═N bond because of the electronic transition from the π orbital of the amine moiety to the π* orbital of the entire molecule, commonly named, the π_2-π_1* transition. [27]

4. Conclusions

The structure of *A-1* was confirmed by single crystal X-ray diffractions studies, thus showing that isomer E is the most stable configuration. Additionally, two conformers where found in the asymmetric unit differing on the rotation of the pyridinic ring over the C_{14}—C_{19} or C_5—C_6 bond. Also, the configurational dynamics of *A-1* was confirmed by the formation of Z isomer when UV light was applied, which was evidenced for the apparition of new signals in the spectrum and specially the one, low field shifted, corresponding to the —NH— being part of a an hydrogen bond. Therefore, it was found that photoisomerization follows a second order kinetics, having a rate constant of $k = 0.147\ M^{-1}\ min^{-1}$.

Determination of optimized structure using *ab initio* methods was achieved with good theoretical–experimental correlation; minimum energy structure (global minima) was demonstrated due to the absence of imaginary frequency in IR theoretical calculations (with good theoretical–experimental correlation). The best interrelation with experimental values was accomplished at DFT: B3LYP/6-311G + level of theory. On the other hand, calculated ^{13}C NMR chemical shift showed acceptable theoretical–experimental correlation ($R^2 = 0.8764$ and 0.8527 for DFT and RHF, respectively) while ^{1}H NMR chemical shift showed unacceptable correlation with experimental data, probably because solvation effect was not included in the calculation method.

Acknowledgments

M.N.C., M.A.G. and G.A.G. greatly thanks the Universidad del Valle, COLCIENCIAS and the Banco de la República for their generous financial support. M.S-M and R. D. Acknowledges FAPESP (2009/54011-8) for provide equipment, Coordenação de Aperfeiçoamento de Pessoal de Nível Superior and Conselho Nacional de Desenvolvimento Cientifico e Tecnológico for the CNPq and CAPES/PNPD scholarships from the Brazilian Ministry of Education.

Appendix A. Supplementary data

Supplementary data related to this article can be found at http://dx.doi.org/10.1016/j.molstruc.2016.04.055.

References

[1] P.T. Corbett, J. Leclaire, L. Vial, K.R. West, J.L. Wietor, J.K. Sanders, S. Otto, Chem. Rev. 106 (2006) 3652–3711.
[2] M.N. Chaur, Acta Crystallogr. Sect. E Struct. Rep. Online 69 (2012) m27–m27.
[3] M.A. Fernández, J.C. Barona, D. Polo-Cerón, M.N. Chaur, Rev. Colomb. Quím. 43 (2014) 5–11.
[4] M.N. Chaur, D. Collado, J.M. Lehn, Chem. Eur. J. 17 (2011) 248–258.
[5] E.L. Romero, R.F. D'Vries, F. Zuluaga, M.N. Chaur, J. Braz. Chem. Soc. 6 (2015) 1265–1273.
[6] APEX2, SAINT, v.6.28A, Bruker-AXS, Madison, WI, 2006. Bruker-Siemens: Madison, WI, 1997.
[7] L.J. Farrugia, J. Appl. Crystallogr. 45 (2012) 849–854.

[8] O.V. Dolomanov, L.J. Bourhis, R.J. Gildea, J.A. Howard, H. Puschmann, J. Appl. Crystallogr. 42 (2009) 339–341.
[9] D. Roy, K. Todd, M. John, Gauss View, Version 5, Semichem, Inc., Shawnee Mission, KS, USA, 2009.
[10] M.J. Frisch, G.W. Trucks, H.B. Schlegel, G.E. Scuseria, M.A. Robb, J.R. Cheeseman, G. Scalmani, V. Barone, B. Mennucci, G.A. Petersson, et al., Gaussian 09, Revision D.01, Gaussian, Inc., Wallingford, CT, USA, 2010.
[11] M.Y. Amusia, A.Z. Msezane, V.R. Shaginyan, Phys. Scr. 6 (2003) C13.
[12] Ochterski, J.W. Vibrational Analysis in Gaussian. Available online: http://www.gaussian.com/.
[13] H. Friebolin, 5th ed.; Wiley-VCH: Weinheim, Germany, 1993, 51.
[14] D. J Hutchinson, L.R. Hanton, S.C. Moratti, Inorg. Chem. 5 (2013) 2716–2728.
[15] G.M. Sheldrick, Acta Crystallogr. Sect. C Struct. Chem. 71 (2015) 3–8.
[16] L.J. Farrugia, J. Appl. Crystallogr. 30 (1997), 565–565.
[17] C.F. Macrae, I.J. Bruno, J.A. Chisholm, P.R. Edgington, P. McCabe, E. Pidcock, L. Rodriguez-Monge, R. Taylor, J. van de Streek, P.A. Wood, J. Appl. Crystallogr. 41 (2008) 466–470.
[18] J.J. McKinnon, M.A. Spackman, A.S. Mitchell, Acta Crystallogr. B 60 (2004) 627–668.
[19] F.L. Hirshfeld, Theor. Chim. Acta. 44 (1977) 129–138.
[20] M.A. Spackman, J.J. McKinnon, CrystEngComm. 4 (2002) 378–392.
[21] A. Ramakrishnan, S.S. Chourasiya, P.V. Bharatam, RSC Adv. 5 (2015).
[22] D. Stöckl, K. Dewitte, L.M. Thienpont, Clin. Chem. 11 (1998) 2340–2346.
[23] J.O. Westgard, M.R. Hunt, Clin. Chem. 3 (2008) 49–57.
[24] M.P. Andersson, P. Uvdal, J. Phys. Chem. A 109 (2005) 2937–2941.
[25] S.M. Landge, E. Tkatchouk, D. Benítez, D.A. Lanfranchi, M. Elhabiri, W.A. Goddard, I. Aprahamian, J. Am. Chem. Soc. 133 (2011) 9812–9823.
[26] J.M. Lehn, Chemistry 12 (2006) 5910–5915.
[27] D.G. Belov, B.G. Rogachev, L.I. Tkachenko, V.A. Smirnov, S.M. Aldoshin, S.M. Russ, Chem. Bull. 49 (2000) 666–668.